Structural, vibrational, and magnetic properties of self-assembled CoPt nanoalloys embedded in SrTiO₃

M. Hennes [1,*,†] E. Fonda [2] N. Casaretto,[1] J. Buchwald [3,‡] X. Weng,[1] G. Patriarche [4] D. Demaille,[1] Y. Zheng,[1] and F. Vidal [1,§]

[1] *Sorbonne Université, CNRS, Institut des NanoSciences de Paris, INSP, 75005 Paris, France*
[2] *Synchrotron SOLEIL, L'Orme des Merisiers Saint-Aubin BP 48, 91192 Gif-sur-Yvette Cedex, France*
[3] *Institute for Materials Science and Max Bergmann Center of Biomaterials, Dresden University of Technology, 01062 Dresden, Germany*
[4] *Université Paris-Saclay, CNRS, Centre de Nanosciences et de Nanotechnologies, 91120 Palaiseau, France*

Pulsed laser deposition was used to synthesize vertically aligned nanocomposites, consisting of ultrathin CoPt nanocolumns embedded in a single crystal SrTiO₃ thin film. Combining high-resolution transmission electron microscopy, x-ray diffraction, x-ray absorption spectroscopy, and molecular dynamics simulations, we provide an in-depth analysis of the structural and vibrational properties of the CoPt phase over a wide range of concentrations. Our findings show that the CoPt nanoalloys are characterized by a high degree of structural disorder and complete absence of chemical ordering, even after additional sample annealing ($T \simeq 670\,°C$). For a Co concentration exceeding $c(\text{Co}) \simeq 0.55$, pole figure measurements unravel a transition from a highly textured short-range disordered fcc phase to a disordered hcp phase with c-axis oriented out of plane, which is at odds with bulk predictions. These findings, further confirmed by magnetometry measurements, illustrate the profound impact of vertical epitaxy on the structural properties of bimetallic CoPt alloys.

I. INTRODUCTION

During the last two decades, a considerable research effort has been devoted to the development of functional oxide thin films with embedded metallic nanostructures. A broad variety of synthesis techniques has been used to grow these hybrid metal-oxide systems: ion implantation [1], low energy cluster beam deposition assisted by co-deposition of the matrix [2–4], ion-irradiation induced viscous flow [5–8], laser treatment [9] or electrodeposition into prestructured templates [10,11] were studied in great detail. However, these approaches still lack the required versatility when one is interested in controlling the nanoarchitecture of the composite system, i.e., the morphology and crystallographic orientation of the embedded metallic structure.

Vertical epitaxy, the three-dimensional counterpart of classical planar epitaxy, has recently emerged as a field of research, with the potential ability to fill this gap. In fact, it has been demonstrated that in mixed metal-oxide systems, nanoscale self-assembly driven by phase separation yields composites with highly tunable crystallographic properties. In addition, careful adjustment of the growth conditions, i.e.

deposition rate, temperature or concentration can be used to achieve precise control over the aspect ratio and morphology of the metallic inclusions [12]. As shown in recent studies, the aforementioned approach seems applicable to a wide range of materials: successful synthesis of epitaxial Fe [13], Co [14–17], Ni [12,18–20], Au [21], Ir [22], Pt, Pd, and Rh [23] nanowire and nanopillar arrays, embedded in different types of oxide matrices has been reported. However, only few experiments on alloy-based composites have been performed yet [24,25]. Within this context, CoPt is a particularly interesting candidate from a fundamental, as well as from a technological point of view. On the one hand, it is an archetypal alloy, which has been studied in detail for its disorder-order phase transitions [26]. On the other hand, some of the ordered phases display a huge uniaxial magnetic anisotropy, which makes them appealing for high density data storage and spintronics applications. Usually, CoPt thin films are grown at room temperature and require subsequent annealing steps to achieve chemical ordering [27,28]. In contrast, the synthesis of vertically aligned metal-oxide nanowire (NW) composites must be performed at high temperatures ($T > 600\,°C$) to activate surface diffusion and achieve substantial phase separation [12]. While this might concomitantly pave the way for the creation of ordered bimetallic phases during growth, it is also well known that chemical ordering can be impeded due to size and shape effects [29]. Matrix atom diffusion into the embedded metals and compound formation can also play an important role and have a detrimental impact on the magnetic properties of CoPt [30,31].

In the present work, we use CoPt-SrTiO₃ (CoPt-STO) as a model system to study the interplay of these effects and analyze whether or not, chemical ordering takes place when

---

ultrasmall nanoalloys self-assemble in a single crystal matrix. Several studies have focused on deposition of CoPt alloy thin films and nanostructures using single crystal SrTiO$_3$ (STO) substrates [32–34]. However, to the best of our knowledge, no data is available yet concerning the possibility to grow metal-oxide composite structures using these materials. In the first part of this paper, we demonstrate that codeposition of Co, Pt, and STO at high temperatures indeed results in self-assembly of nanocolumnar metal-oxide thin films. We then turn to an in-depth description of their peculiar structural and magnetic properties before closing with a conclusion and outlook.

II. MATERIALS AND METHODS

A. Sample preparation

CoPt-STO thin films were grown by sequential pulsed laser deposition on STO(001) substrates, using Pt, CoO and STO targets. A quadrupled Nd:YAG laser (wavelength 266 nm) was employed, operated at 10 Hz with a fluence in the 1–3 J/cm^2 range. The temperature of the substrate during growth was close to 650 °C, the base pressure in the UHV chamber was below 2×10^{-9} mbar, the pressure during growth did not rise above 5×10^{-7} mbar. The general growth procedure consisted in a repetition of one basic deposition sequence, with alternating laser shots on STO, CoO and metallic Pt targets [Fig. 1(a)]. The total number of laser shots in one sequence, as well as the total number of laser shots $n_{Pt} + n_{CoO}$ was kept constant, while the ratio n_{Pt}/n_{CoO} was changed systematically, to obtain samples with varying concentration. A thin STO capping layer of 2–3 nm thickness was deposited to protect the NWs from oxidation. Detailed information on the synthesis procedure and the underlying mechanisms giving rise to nanocomposite growth can be found in earlier publications [24], especially in Ref. [12], where a detailed description of the early stages of NW growth in Ni-STO thin films is provided using kinetic Monte Carlo and density functional theory

calculations (DFT) combined with experiments. Recent DFT calculations suggest that these results also apply to CoPt-STO nanocomposites [35].

B. Structural and magnetic measurements

The structure of the samples was studied using a combination of techniques including transmission electron microscopy (TEM) and scanning transmission electron microscopy (STEM), x-ray diffraction (XRD), and x-ray absorption spectroscopy (XAS). High resolution transmission electron microscopy (HRTEM) data were acquired using a JEOL JEM 2100 F equipped with a field-emission gun operated at 200 kV. STEM data were gathered using a Titan Themis 200. The surface structure of the samples was analyzed using a Zeiss Ultra55 scanning electron microscope (SEM). Energy-dispersive x-ray spectroscopy (EDX) was used to map the chemical distribution of the elements using all three electron microscopes mentioned above. X-ray diffraction (XRD) and x-ray reflectivity (XRR) data were obtained on a laboratory diffractometer (Rigaku SmartLab) with Cu K$_{\alpha 1}$ radiation (wavelength of 1.54 Å). Co K-edge and Pt L_3-edge XAS data were collected at the beamline SAMBA (Synchrotron SOLEIL). All samples were probed in fluorescence detection mode. A commercial vibrating sample magnetometer system was used to record temperature-dependent magnetization curves (PPMS, Quantum Design) in in-plane and out-of-plane geometry.

C. MEAM-based MD simulations

Classical molecular simulations were carried out with the LAMMPS [36] code using a cell containing 2916 atoms and periodic boundary conditions. The interactions between the atoms were described in terms of the second nearest-neighbor modified embedded atom method (MEAM) [37] using the parametrization of Kim *et al.* [38]. After 10 ps equilibration of the cell to a mean pressure of 0 bar within the *NPT* ensemble, a run was conducted within the canonical ensemble
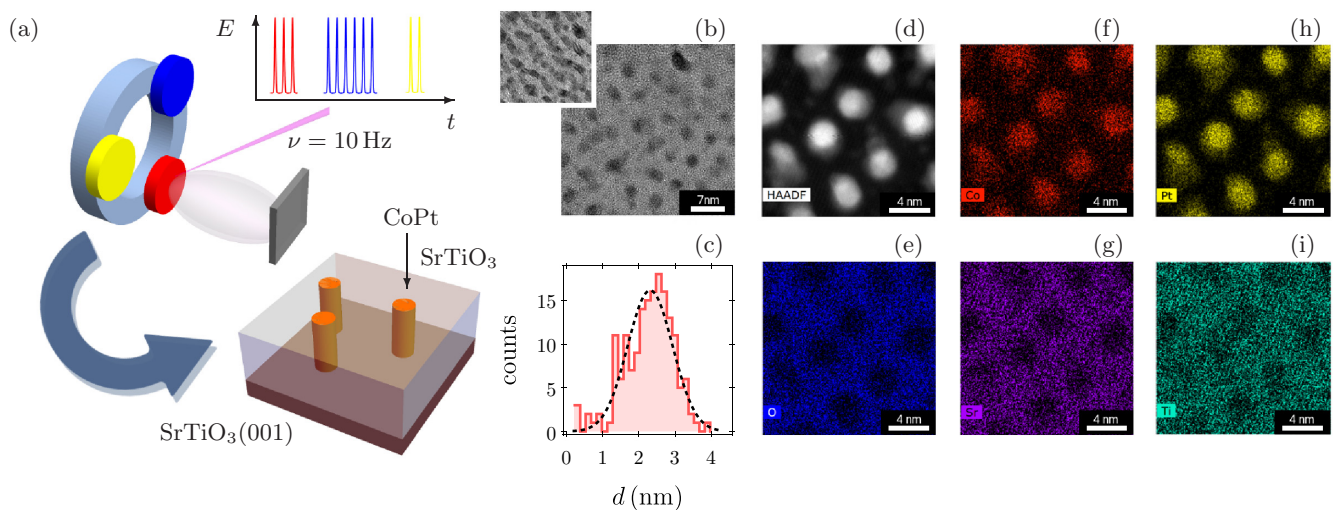

FIG. 1. Schematics of the growth procedure and exemplary electron microscopy data. (a) Sequential pulsed laser deposition using Pt, CoO and STO targets, results in growth of CoPt-STO nanocomposites. (b) HR-TEM plan view and tilted view, which unravels the columnar morphology of the nanoinclusions in the single crystal STO matrix. (c) Diameter distribution of the embedded structures (sample S4). (d)–(i) plan view STEM-HAADF and EDX data gathered on sample S1 (red: Co, yellow: Pt, blue: O, magenta: Sr, green: Ti) provide detailed chemical information on the nanocomposite and confirm phase separation and creation of CoPt nanoalloys.

TABLE I. Structural parameters and composition of the Co_xPt_{1-x}-STO samples. Average nanorod diameters $\langle D \rangle$ determined from plan view TEM micrographs, sample thickness t obtained via XRR. Concentrations measured via SEM-EDX (c_I), HRTEM-EDX (c_{II}) and STEM-EDX (c_{III}).

| Sample | $\langle D \rangle$ (nm) | t (nm) | c_I (at. %) | Co concentration | |
				c_{II} (at. %)	c_{III} (at. %)
S0	2.5 (5)	73	0	0	-
S1	2.5 (4)	66	20 (2)	25	15(5)
S2	3.5 (9)	57	42 (4)	42	32(4)
S3	2.6 (6)	76	51 (2)	52	-
S4	2.7 (7)	44	57 (5)	57	
S5	2.4 (8)	73	57 (3)	63	48(3)
S6	2.6 (6)	57	67 (2)	75	-
S7	1.8 (8)	32	100	100	-

at 300 K using Nosé-Hoover thermostating [39,40]. All runs were performed over a time span of 100 ps with a time step of 1 fs.

III. RESULTS AND DISCUSSION

A. Bimetallic nanopillar formation

We start this section by providing evidence for phase separation and nanopillar formation in the CoPt-STO thin films. Figure 1(b) shows a representative HR-TEM image of sample S4. In this plan view, nanoinclusions with irregular but mostly disklike shape can easily be identified. Tilting of the sample ($\theta = 25°$) revealed the columnar morphology of the nanocomposite [inset of Fig. 1(b)], which has been found in all samples, irrespective of concentration. The number densities and diameters of the embedded structures were quantified using Mathematica®-based image processing scripts, which permitted us to analyze a large number of plan view micrographs (a detailed summary of the results obtained for various Co and Pt concentrations is given in Table I). The porosity of the samples, i.e., the ratio of nanowire and total film volume, was equal to $17 \pm 4\%$. The average diameters of the columns were found to lie roughly between 2 and 3.5 nm, with no systematic change upon variation of the concentration. Figure 1(c) shows an exemplary diameter distribution obtained on sample S4. While the latter exhibits an overall Gaussian shape, slight deviations become apparent for small diameters. Indeed, in all samples, a second peak, typically below $d \simeq 1.5$ nm, is observed, hinting at a small amount of additional buried structures. This is confirmed by careful analysis of STEM-high-angle annular dark-field (HAADF) maps, which provide better contrast due to high Z sensitivity. As shown in Fig. 1(d), small clusters with faint contrast located in between the pillars can be identified.

To complement our morphological analysis, quantitative EDX data of the thin films were acquired with different spatial resolution, giving access to chemical information on various length scales (Table I). Low resolution maps, were obtained by using SEM-EDX and scanning point arrays over the entire sample to improve the statistics. EDX data gathered with

this approach unraveled the lateral homogeneity of the thin films. This was further confirmed by using HRTEM-EDX. Data obtained when scrutinizing thin film regions containing several thousand NWs (typical length scales close to 100 nm) were found in very good agreement with the aforementioned results. In addition, samples S1, S2, and S5 were analyzed in greater detail using STEM-HAADF and STEM-EDX, providing chemical information down to sub-nm length scales. As exemplified in Figs. 1(e)–1(i), the columnar inclusions display strong Co and Pt signals, correlating with low Sr, Ti, and O intensities. This provides strong evidence for phase separation and creation of CoPt alloy nanostructures. Surprisingly, STEM-based quantitative chemical analysis of embedded metallic CoPt yielded systematic concentration deviations of roughly 10–15%, when compared to the low resolution EDX data: all samples appear to be slightly Co deficient (Table I). This holds true for isolated CoPt columns as well as for larger matrix-nanowire composite regions (probed lateral length scales of approximately 10 nm), which display almost identical concentrations. Thus, the observed discrepancy cannot be attributed to cobalt enrichment in the surrounding STO. To resolve this apparent contradiction, it is necessary to recall that STEM-EDX mapping not only yields a highly local chemical analysis of the sample in plane, its vertical sensitivity also differs from the two aforementioned EDX techniques. In fact, only the upper 10–15 nm of the thinned film were probed in order to achieve ideal electron beam transparency. In contrast, the SEM-EDX and HRTEM-EDX analysis presented above allowed to assess the chemical composition of the composite thin film from its surface down to the substrate interface. The observed differences thus hint at a weak concentration gradient in the thin films, which appear to be slightly Co enriched at the substrate interface, while presenting a larger Pt concentration at their surface. Finally, quantitative chemical analysis of the matrix indicates that, within measurement uncertainty, the concentration of Ti, $c(Ti)$, approximately equals the concentration of Sr, $c(Sr)$ and we obtain $c(Ti) \simeq c(Sr) \simeq 1/3 \cdot c(O)$. This is in agreement with the expected formation of STO and further confirmed by our TEM data as well as XRD measurements, that will be presented in a later part of this work. Note that the presence of minute amounts of Sr, Ti and O on top of Co and Pt in plan view, as seen in Fig. 1(d), results from the thin STO capping layer, used to prevent oxidation and contamination.

B. Alloying and absence of chemical short range ordering

While the combined SEM, TEM, and EDX analysis, presented in the last section, allows us to conclude that shape anisotropic CoPt-rich inclusions are formed inside the STO matrix during growth, they provide little information on a possible oxide or compound creation in the matrix/nanorod interface region. In addition, EDX mapping does not allow us to discriminate between chemically ordered and disordered phases. To complement our structural analysis, we therefore performed x-ray absorption spectroscopy measurements that will be presented in the following paragraphs.
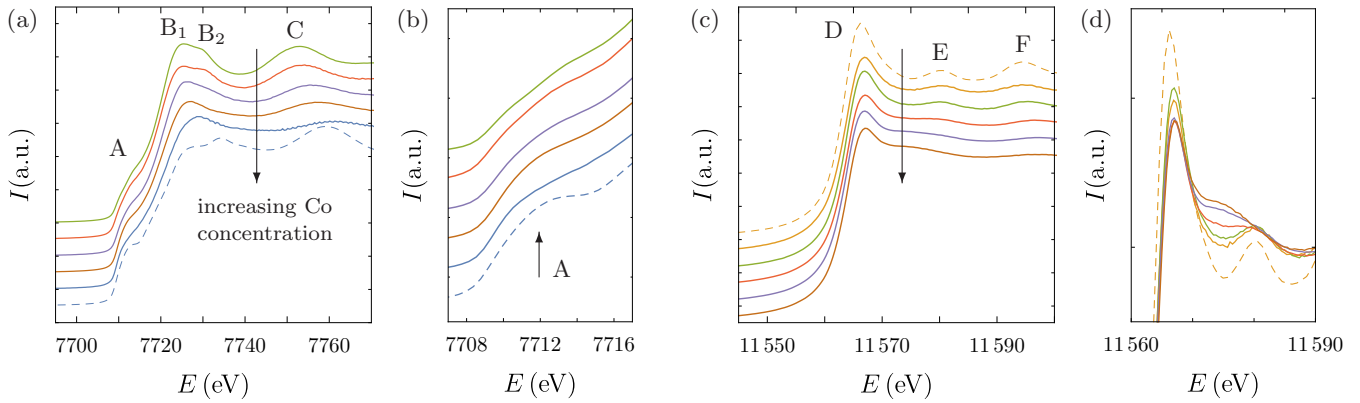
FIG. 2. XANES data obtained at the Co *K*- and Pt *L*$_3$-edges (increasing Co concentration from top to bottom) and main features labeled from A to F: Co and Pt foils (dashed blue and dashed orange, respectively) and samples S7 (blue), S6 (brown), S4 (purple), S2 (red), S1 (green) and S0 (orange). (a) Co *K*-edge, (b) magnified spectra illustrating the decreasing magnitude of peak A with increasing Pt concentration. (c) Pt *L*$_3$-edge and (d) zoom on the white line. Note that the curves in (a)–(c) were shifted vertically for clarity.

1. X-ray absorption spectra (XAS) of as-deposited samples

Figure 2 shows x-ray absorption near edge spectra (XANES) recorded at the Co *K*-edge and Pt *L*$_3$-edge for nanocomposites with varying Co and Pt concentration, as well as reference spectra measured on Co and Pt foils. At the Co *K*-edge, three distinct features (labeled A, B, and C) can be identified in the near-edge region [Fig. 2(a)]. Peak A reflects transitions from 1*s* core levels to unoccupied states exhibiting mainly 3*d* character while the peak B results from final configurations with 4*p* character [41–44]. Previous work has evidenced that the magnitude of these local maxima in CoPt alloys depends on the concentration, reflecting their sensitivity upon modifications in the alloy electronic density of states. As can clearly be inferred from Fig. 2(b), the magnitude of peak A decreases with increasing Pt concentration in the samples. This behavior agrees with data reported in earlier studies [41,42,45] and has been explained theoretically by an increase in 3*d* electron occupancy at Co sites when increasing the Pt concentration. In contrast, the feature B is less straightforward to analyze in the present case. While a reduction in peak intensity with increasing Co concentration was demonstrated (and traced back to a reduction of 4*p* states resulting from an alloying induced weakening of *p*-*d* hybridization at Co sites [42]), our data reveal a concomitant change of the peak shape with concentration. Indeed, for high values of *c*(Pt), B is composed of two maxima *B*$_1$ and *B*$_2$, which arise from band structure effects. These separated structures merge into one with increasing *c*(Co), which suggests a loss of crystallinity in the NWs with higher Co concentration [20]. Finally, peak C can be attributed to fine structure oscillations: with increasing Pt content, a shift towards lower energies (larger interatomic distances) is observed. A detailed analysis of the extented x-ray absorption fine structure (EXAFS) part of the spectrum will be given in the next section. At the Pt *L*$_3$-edge, differences between the spectra are less pronounced [Fig. 2(c)]. The most prominent feature in the Pt XANES is the white line, reflecting 2*p*$_{3/2}$ → 5*d*$_{5/2}$ transitions [46] [peak D in Fig. 2(c)]. As shown in Fig. 2(d), superposition of the spectra reveals a decrease of the white line intensity and broadening with increasing Co concentration. This effect is rather small and

saturates around 40% Co concentration, in agreement with literature data [42].

While XANES confirm phase separation and growth of metallic CoPt structures embedded in STO, they do not provide details on the degree of ordering of the alloy [47]. In contrast, analysis of the fine structure permits us to gather information on the type and the number of neighboring atoms, as well as on distances separating the absorber and the scatterer [48]. For data analysis, the IFEFFIT libraries were used [49]. Raw spectra were treated with ATHENA to remove the background and glitches and to normalize the data. ARTEMIS was then used for quantitative EXAFS fitting. To achieve maximum consistency, an identical analysis procedure was applied to all samples. Measurements on Co and Pt foils were first used to calculate the amplitude reduction factor S_0^2 [$N = 12$, S_0(Co) $= 0.8 \pm 0.02$ and S_0(Pt) $= 0.86 \pm 0.03$]. We then fitted all nanocomposite spectra by assuming Co and Pt atoms to be exclusively surrounded by either Co or Pt neighbors. In these calculations, only next neighbors (n.n.), i.e., the first coordination shell was taken into consideration. Fourier transformations of $\chi(k)$ spectra were performed in the range 3 Å^{-1} < k < 11 Å^{-1} using a Hanning window with $dk = 1$ Å^{-1}. Six modeling parameters per edge were used: an energy correction factor ΔE, two n.n. distances d (one for each type of neighbor), two total n.n. numbers N (N_{Co} and N_{Pt}) and one Debye-Waller factor σ. While, for the present system, it would seem advisable to choose different disorder parameters to describe Co-Pt and Co-Co as well as Pt-Co and Pt-Pt bonds, this approach did not result in a consistent fitting of the data and produced large errors. We, therefore, stuck to a single EXAFS Debye-Waller parameter σ per edge in the first place. Similarly, we found that a third cumulant C_3, usually employed in nanoscale systems as a correction for non-Gaussian distance distributions, did not improve the fits and no clear evolution of C_3 with concentration could be identified.

Figures 3(a) and 3(b) show $\chi(r)$ data obtained by Fourier transformation of k^2 weighted $\chi(k)$ spectra gained on CoPt alloy composites together with corresponding fits. Co and Pt foils and elemental nanocomposites are presented as well. In general, the agreement between the measured data and fits
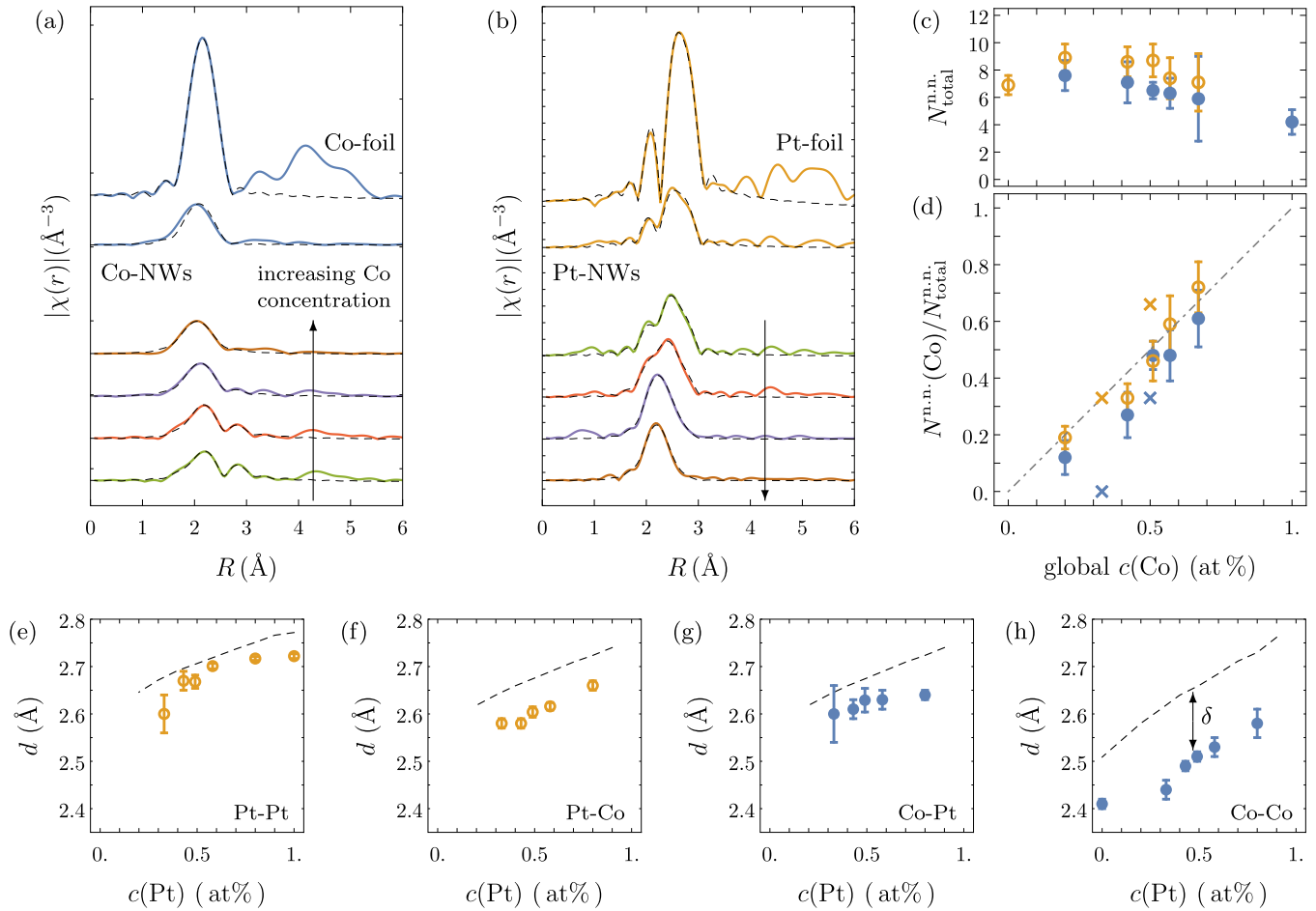
FIG. 3. EXAFS measured on nanocolumnar CoPt-STO samples with varying Co/Pt ratio (arrows indicate increasing Co concentrations). Co and Pt foil data are shown for comparison. $\chi(r)$ data obtained after Fourier transformation of $k^2\chi(k)$ at the (a) Co K-edge and (b) Pt L_3-edge (same color coding as in Fig. 2) as well as corresponding fits (black dashed line). (c) Total number of next neighbors (n.n.) as a function of concentration, (d) local Co concentration vs global Co concentration (crosses indicate the values expected for pure $L1_0$ and $L1_2$ phases), n.n. distances for (e) Pt-Pt, (f) Pt-Co, (g) Co-Pt and (h) Co-Co bonds (blue solid points: Co K-edge, orange circles: Pt L_3-edge, black dashed line: MEAM results).

is good. However, quantitative analysis of the measurements reveals that the CoPt alloy exhibits some rather peculiar features. First, note that the total number of next neighbors is much smaller than what is expected for a bulk fcc metal ($N = 12$), which is shown in Fig. 3(c). In addition, we also find systematic variations with concentration and edge type: the coordination number decreases almost linearly with Co concentration. At the same time, the overall number of next neighbors seems to be slightly larger at the Pt edge. Knowledge of the number of next neighbors of each type allows us to calculate a local concentration and can be used to assess the degree of short- range ordering. As becomes clear in Fig. 3(d), neither $L1_2$ nor $L1_0$ phases (expected values for perfect short range order are marked with crosses for both edges) can be evidenced. Within measurement uncertainty, local Co and Pt concentrations, i.e., the number of Co neighbors surrounding either a Pt or Co atom, are identical and match the global concentration, which yields strong evidence for random mixing of the constituents [26]. This can additionally be checked by analyzing the n.n distances. Considering the alloy to be chemically disordered, we expect d to increase

monotonuously with the Pt content [26]. This is indeed what we observe, as shown in Figs. 4(e)–4(h). Note that we find an identical behavior for Co-Pt bond lengths at the Co and at the Pt edge, which illustrates the viability of our fit strategy. These experimental bond lengths resulting from our EXAFS fits can finally be compared with theoretical predictions. In the present case, we calculated the expected concentration dependent values of d_{Co-Co}, $d_{Co-Pt} = d_{Pt-Co}$ and d_{Pt-Pt} for a randomly alloyed CoPt bulk system using MD simulations based on the MEAM. The results are shown in Figs. 3(e)–3(h). While very good agreement of the differential increase $dd/dc(Pt)$ is observed, all experimental data display a constant offset δ. The discrepancy found for Pt-Pt bond lengths is rather small ($\delta \simeq 0.03$ Å), it increases for CoPt bonds ($\delta \simeq 0.08$ Å) and becomes as large as $\delta \simeq 0.15$ Å for Co-Co bonds, a relative contraction of approximately 6%.

2. In situ annealing experiments

The absence of chemical ordering, the small coordination numbers as well as the bond-length contractions described in
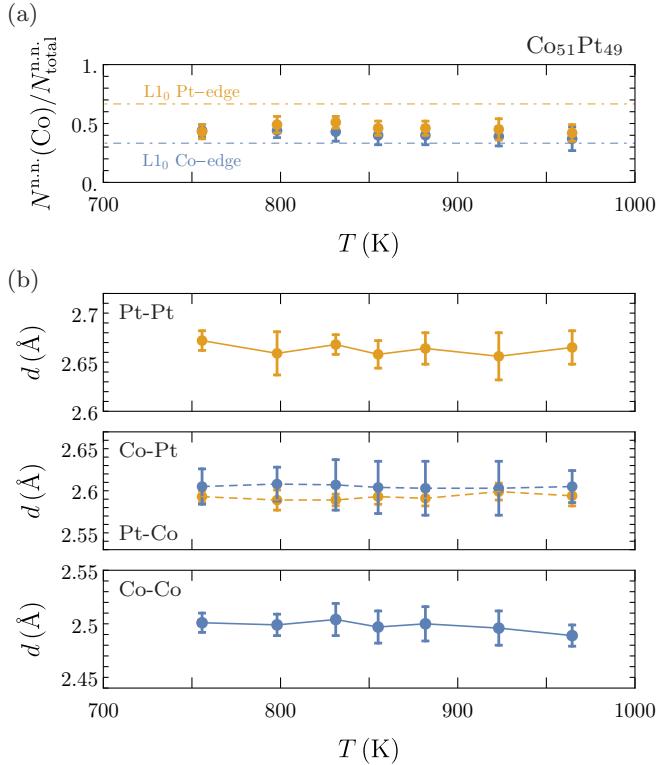
FIG. 4. *In situ* annealing study performed on sample S3, using annealing times $t_a^\star = 10\,\mathrm{h}$ (at 750 K) and $t_a = 2\,\mathrm{h}$ for all other temperatures. (a) Local Co (n.n) concentration (blue dots: Co K-edge, orange dots: Pt L_3-edge, dashed dotted lines: expected values for an ideal L1$_0$ phase) and (b) n.n distances as a function of T (same color coding as before).

the previous paragraph require closer analysis. In a first step, in order to check for a possible quenching of as-deposited samples into metastable, far from equilibrium states (e.g., due to rapid cooling at the end of the growth process), we complemented our experiments with an *in situ* XAS annealing study performed on sample S3, which is characterized by almost equiatomic composition (Co$_{51}$Pt$_{49}$). As shown in Fig. 5, the data gained upon annealing up to 1000 K ($t \simeq 2$ h and $T \simeq 600\,^\circ$C are typically employed to achieve L1$_0$ ordering in CoPt thin films), do not hint at significant changes in the lattice parameters, nor do they provide any evidence for a pronounced, systematic evolution of the system. A very small decrease of the relative amount of Co n.n. is observed at the Pt as well as at the Co edge and might be ascribed to partial Co oxidation. In fact, the appearance of a shallow peak at small distance in the $\chi(r)$ data supports this hypothesis.

3. Vibrational properties and Debye-Waller factor

Besides giving access to changes in local order and average interatomic distances, our annealing study also provides information on the vibrational properties of the nanoalloy via calculation of the temperature dependent Debye-Waller factor $\sigma(T)$. This yields a valuable consistency check for our EXAFS analysis, as the aforementioned contraction of bond lengths should also become manifest in a change of the vibrational signature of the system. Using the equipartition
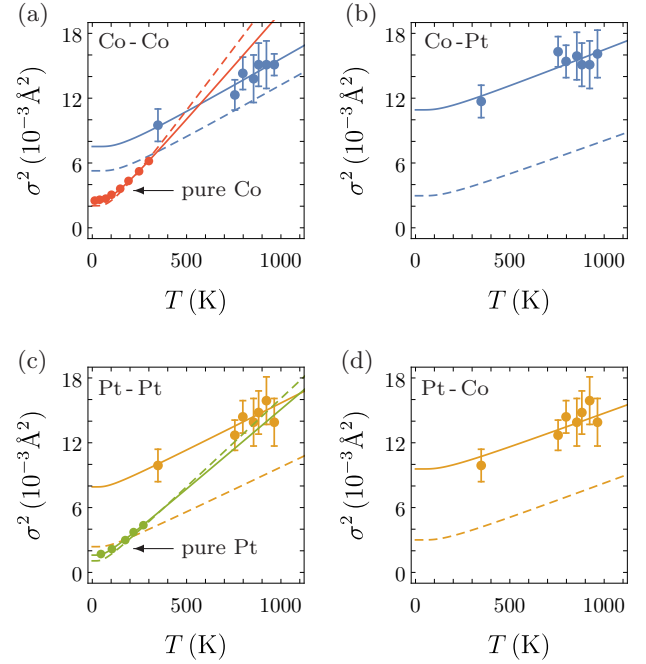

FIG. 5. Evolution of the Debye-Waller EXAFS parameter σ^2 with temperature. Measurements performed at the (a),(b) Co K-edge (blue) and (c),(d) Pt L_3-edge (orange) as well as literature data gained on pure Co and Pt systems (red and green) and fits to Eq. (1) (fits to MEAM simulations: dashed lines, fits to experimental data: solid line).

theorem, a link between the characteristic frequency of an ensemble of uncoupled, quantized harmonic oscillators with energies $E_i = n_i(\hbar\omega_E + 1/2)$, i.e., the Einstein model, and the width of the distribution of interatomic distances σ is readily established:

$$\sigma^2(T) = \frac{\hbar}{M\omega_E} \coth(\beta\hbar\omega_E/2). \tag{1}$$

Here, M denotes the reduced mass of the absorber-scatterer pair, ω_E, the Einstein frequency, and $\beta = 1/k_BT$. For ease of comparison with literature values, we used a frequency to temperature conversion: $k_B\theta_E = \hbar\omega_E$. This approach has been used extensively in EXAFS analysis and usually results in a rather good description of the experimental data, as $\sigma(T)$ is not impacted by the details of the phonon density of states [48].

We adopted the textbook approach for description of $\sigma(T)$ and decomposed the latter into a dynamic and a temperature independent static part: $\sigma(T)^2 = \sigma_s^2 + \sigma_d(T)^2$. In contrast to the strategy used in the last section, EXAFS data were fitted using two different σ values. Calculated EXAFS σ_{Co-Co}, σ_{Co-Pt}, σ_{Pt-Co} and σ_{Pt-Pt} as well as fits to the experimental and MEAM results using Eq. (1) are shown in Fig. 5 (Table II provides a survey of the calculated Einstein temperatures). A comparison of our MEAM modeling with EXAFS literature data gained on bulk Co and Pt shows good agreement and underpins the validity of our approach. As expected, $\sigma(T)$ of the alloy differs significantly from the aforementioned elemental data. While the values show significant scattering (which results from the use of two different σ values at each edge)

TABLE II. Einstein temperatures θ_E(K): bulk literature values for Co and Pt [50,51] and calculated data for the present CoPt nanoalloy. MEAM results are given in parenthesis.

	Bond type	Co edge	Pt edge
Co bulk hcp/fcc	Co-Co	295/286 (265)	–
Pt bulk	Pt-Pt		179 (173)
CoPt-STO	Co-Co	405 (409)	–
	Co-Pt	396 (412)	416 (412)
	Pt-Pt	–	242 (248)

the Einstein temperatures deduced from our experiments are very close to the bulk MEAM predictions (Table II). Within experimental uncertainty, the nanoalloy thus behaves as a bulk system. This finding is at odds with the pronounced bond length shortening described in a previous section of this paper, which should result in a shift of the characteristic frequency to higher values. As will be shown in the next section, a closer analysis of the static Debye-Waller factor σ_s might provide the key for a better understanding of the XAS data.

4. Structural disorder

As can be seen in Fig. 5, a comparison of our experimental CoPt data with MEAM-based simulations show a large constant offset, i.e., unexpectedly large σ_s values revealing the presence of pronounced structural disorder. In fact, detailed analysis of the XAS data confirms this observation. A subtle hint at the poor crystallinity of the CoPt phase has already been identified in the XANES, where, at the Co edge, the double peaks B1 and B2 merge into a single maximum with increasing Co concentration [20,52]. Note that a similar vanishing of the double peak was reported in experiments on $Co_{50}Pt_{50}$ nanoparticles with sizes of approximately 2 nm [45]. Further qualitative confirmation for the low degree of crystallinity can be obtained by closer inspection of the Fourier transformed $\chi(r)$ spectra. As shown in Figs. 3(a) and 3(b), all information beyond the first coordination shell is averaged out and the spectra become essentially flat. The effect becomes more pronounced with increasing Co concentration, it therefore seems not plausible to link it to a concentration gradient in the sample. More likely, this observation results from a severe loss of structural order, as has been reported in studies dealing with amorphous ultrathin films [53], irradiated nanoparticles [52], and ultrasmall embedded NWs [20]. This is further supported by the small coordination numbers and shifts in n.n. distances observed in our EXAFS analysis. At first glance, the bond length contractions might be conceived as a consequence of the small size of the bimetallic inclusions. Indeed, capillary pressures are well known to induce bond length changes up to several percent [54]. However, the diameters of the rods appears too large to induce such strong shifts. In addition, the behavior of embedded structures is expected to be different from freestanding clusters as they do not exhibit a free surface but an interfacial layer with epitaxial coupling to the matrix, going along with the creation of metallic bonds [55]. Furthermore, as shown in the last section, we find no evidence for bond stiffening, which should result from a reduction of the interatomic distances. The coordination

numbers shown in Fig. 3(c) are even more striking. While they are close to ten at the Pt edge for higher Pt concentrations (which appears reasonable for such small nanowires considering their high surface to volume ratio), we observe a pronounced decrease with Co concentration. Especially at the Co edge, the values become too small to be explained by finite size effects. It is clear that neither the few clusters seen in TEM nor minute amounts of Co atoms incorporated into the matrix can induce such a behavior. As already highlighted, we find no evidence for Co oxidation and we also emphasize that the data cannot be fitted by taking interdiffusion of matrix elements such as Ti into consideration. The poor crystallinity of the embedded CoPt phase can however provide an explanation for these observations. In fact, large degrees of structural disorder are known to induce a breakdown of the Gaussian approximation used for EXAFS fitting, which can result in an underestimation of n.n. distances and coordination numbers [48]. In the present case, the disordering appears to be quite pronounced, as the use of higher cumulants did not yield any improvement of the fits. As will be shown in the next paragraph, characterization of the samples *via* XRD further underpins this hypothesis and suggests a progressive and important loss of crystallinity of the embedded phase with increasing Co content.

C. Matrix-induced fcc → hcp transitions

1. X-ray diffraction (XRD) analysis

In addition to the HR-TEM and XAS measurements presented so far, we collected XRD data, combining $\theta - 2\theta$ scans and pole figure measurements to gain additional information regarding the crystallographic properties of our samples. $\theta - 2\theta$ data confirm the homoepitaxial growth of STO on the single crystal substrate (data not shown) and corroborate our HR-TEM analysis. The scans also provide information on the embedded CoPt phase. A shallow, broad peak attributed to diffraction from CoPt (111) planes is observed around $2\theta \simeq 41°$ and shifts with concentration. The derived lattice parameters follow bulk predictions [26] and we find no evidence for large out-of-plane (OP) strains that were reported in systems with pure cube-on-cube epitaxy, such as Ni or CoNi nanowires in STO [20,25,56]. In fact, in the present system, a more complex epitaxial relationship between the matrix and the nanoalloy was identified. Figure 6 shows pole figure measurements performed on a Pt- and a Co-rich nanocomposite (S1 and S4, respectively). As can be seen in Figs. 6(a)–6(c), the Pt-rich sample is characterized by a pronounced texturing of the metallic phase. The data can be well reproduced by using three crystallite orientations: the cube-on-cube orientation and two four-fold degenerated ones obtained by a rotation around the $[-110]_{STO}$ axis leading to $[111]_{CoPt}//[110]_{STO}$ and $[11-1]_{CoPt}//[111]_{STO}$, respectively (i.e., obtained by a 35.26° and −70.52° rotation around the $[-110]_{STO}$, respectively), as shown in Fig. 6.

Surprisingly, the texture changes dramatically with increasing Co content of the samples, as can be seen by comparing Figs. 6(a)–6(c) with 6(d)–6(f). While the intensity of the poles decreases gradually until reaching approximately $c_{crit}(Co) \simeq 0.55$ (which provides additional support for a decreased degree of crystallinity) fundamental
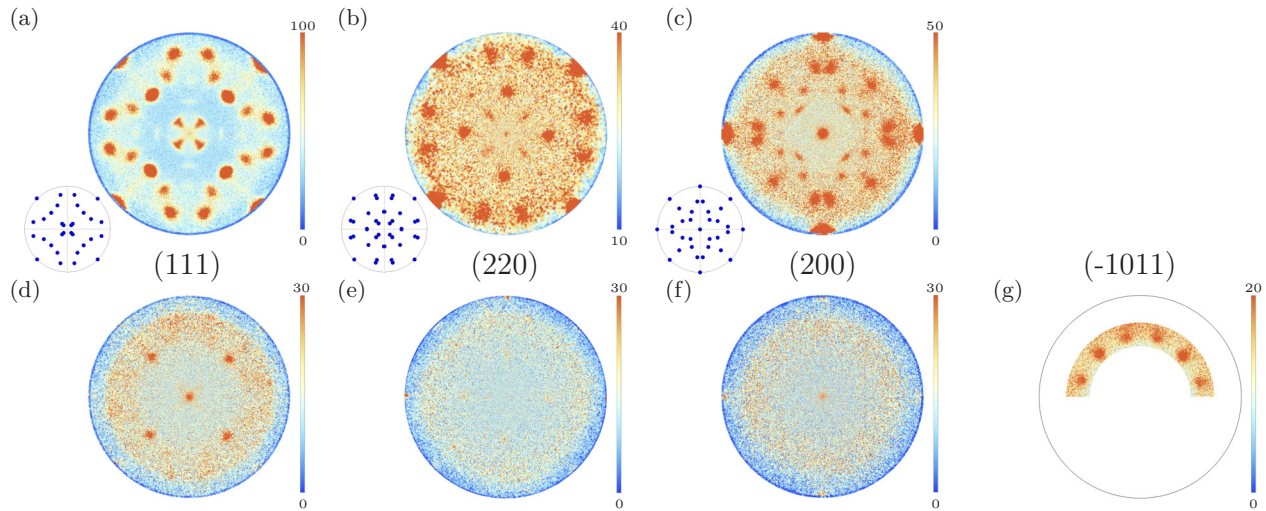
FIG. 6. Pole figure measurements. (a)–(c) (111), (220) and (200) poles in a Pt-rich sample (S1) as well as predictions using three different crystallite orientations (inset). (d)–(g) (111), (220) (200) and (-1011) poles in a Co-rich sample (S4).

structural changes occur once the aforementioned critical Co concentration is reached. While almost all information is lost in the (220) and (200) pole figures, the (111) pole figure shows faint peaks corresponding to a cube on cube epitaxy with an additional central pole. The latter is the signature of an unexpected hcp phase with c axis oriented out of plane. This becomes apparent in Fig. 6(g), where hcp (-1011) peaks [Fig. 6(g)] with 12-fold symmetry can clearly be identified. Note that this observation is further corroborated by our HR-TEM data, where characteristic lattice spacings corresponding to a chemically disordered CoPt hcp phase were identified (data not shown).

2. Magnetic anisotropy

The columnar structure of the embedded CoPt phase, as well as the concentration dependent fcc $\rightarrow$ hcp texture changes evidenced in the last section, are both expected to have a marked impact on the magnetic anisotropy of the composite. Analysis of the magnetic properties of the CoPt-STO thin films as a function of the composition thus provides supplementary information that can be linked to the structural and morphological data presented so far. Temperature dependent magnetization curves were gathered on samples S1–S5. Exemplary results are shown in Figs. 7(a) and 7(b) (samples S3 and S5) for IP and OP configurations [Fig. 7(c)]. At room temperature, all nanocomposites exhibit superparamagnetic behavior ($5\,\mathrm{Oe} \lesssim H_c \lesssim 20\,\mathrm{Oe}$), while at 10 K, the ferromagnetic characteristics are retrieved. Pt-rich samples exhibit coercive fields $2\,\mathrm{kOe} \lesssim H_c \lesssim 3\,\mathrm{kOe}$, which increase slightly with Co concentration. Beyond c_{crit}, the hysteresis loops change dramatically. As shown in Fig. 7(b), the low temperature OP data hint at a much larger coercive field $H_c \gtrsim 10\,\mathrm{kOe}$. In addition, we observe a small "shoulder", which suggests that the sample is composed of two different populations of magnetic nano-objects with soft and hard magnetic properties, respectively. Qualitatively, this is in agreement with our structural analysis: at low concentrations, the samples consist of chemically disordered fcc-

textured nanowires and present a moderate anisotropy, which results mainly from the high aspect ratio of the embedded structures. Above c_{crit}, a partial fcc $\rightarrow$ hcp transformation occurs, possibly accompanied by an amorphization of parts of the nanoalloy [20]. The c axis of the hcp phase, an easy magnetization axis, is oriented in the OP direction which gives rise to a pronounced anisotropy increase. To assess this quantitatively we calculated the anisotropy of the system *via* $K_{\mathrm{eff}} = \mu_0 \int_0^{H_s} dH(M_\perp(H) - M_\parallel(H))$. The values are shown in Fig. 7(c). For small Co concentrations, a uniaxial anisotropy based solely on magnetostatic contributions $K_{\mathrm{ms}} = \frac{\mu_0}{4}M_s^2(1 - 3p)$ provides a reasonable description of K_{eff}. Deviations occur, among other things, from the difficulty to correctly determine the porosity p of the sample. Note also that the fcc phase has an easy axis along the [111] direction, but is magnetically rather soft and thus, has little impact on the final value of K_{eff} [57]. In contrast, for Co concentrations above c_{crit}, an increase of K_{eff} by a factor of more than two is seen, which is clearly too large to be rationalized by the slow growth of K_{ms} with Co content. We ascribe this jump to a magnetocrystalline contribution to the energy of the system, which stems from the creation of a significant amount of hcp CoPt. Note that we do not see any pronounced temperature dependence of K_{eff}, as would be expected for pure hcp Co, where $K_{\mathrm{mc},1}$ is nearly halved when increasing the temperature from 10 to 300 K [58]. Unfortunately, data describing the magnetic properties of chemically disordered CoPt alloys are scarce. Magnetocrystalline anisotropy constants of hcp CoPt have been determined by Bolzoni *et al.* [59]. For bulk CoPt, the hcp phase is found stable in a concentration range $0.8 \lesssim c(\mathrm{Co}) < 1$ with $0.6\,\mathrm{MJ/m^3} \lesssim K_{\mathrm{mc},1} + 2K_{\mathrm{mc},2} \lesssim 1.1\,\mathrm{MJ/m^3}$. To assess these constants independently, we fitted our IP data at 300 K using a simple hard axis magnetization model [60], considering exclusively magnetostatic and magnetocrystalline contributions: $\mu_0 H(m)M_s = 2(K_{\mathrm{mc},1} + K_{\mathrm{ms}})m + 4K_{\mathrm{mc},2}m^3$, with $m = M/M_s$ and $K_{\mathrm{eff}} = K_{\mathrm{mc},1} + K_{\mathrm{mc},2} + K_{\mathrm{ms}}$. From the fit, we get $K_{\mathrm{mc},1} = 2.3 \cdot 10^5\,\mathrm{J/m^3}$ while $K_{\mathrm{mc},2} = 1.5 \cdot 10^5\,\mathrm{J/m^3}$, and
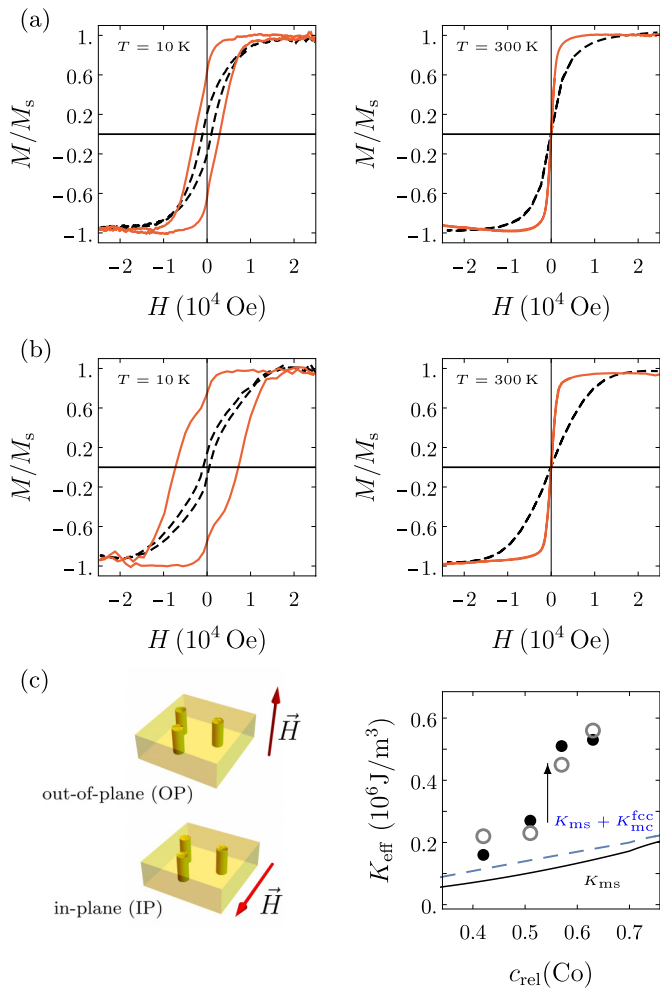
FIG. 7. Temperature dependent magnetometry measurements: (a) At 10 K (left) and 300 K (right) in IP (black dashed line) and OP geometries (red solid line) below c_{crit} (sample S3) and (b) At 10 K (left) and 300 K (right) in IP (black dashed line) and OP geometries (red solid line) above c_{crit} (sample S5). (c) IP and OP measurement geometries employed in this work (left). Effective uniaxial anisotropy K_{eff} calculated from the magnetization loops at 10 K (gray circles) and 300 K (black dots). The magnetostatic anisotropy K_{ms} (black solid line) and magnetocrystalline K_{mc} fcc contributions (blue dashed curve) are shown as well (right).

thus $K_{mc,1} + 2K_{mc,2} \simeq 0.5 \, \text{MJ/m}^3$. This is compatible with the data provided by Bolzoni *et al.* and thus provides additional quantitative evidence for the creation of the hcp CoPt phase.

IV. CONCLUSION

To summarize, we showed that sequential deposition of sub-monolayer amounts of Co, Pt, and STO on STO(001) substrates results in self-assembly of nanocomposites, with ultrasmall, shape anisotropic bimetallic CoPt nanoalloys, ver-

tically embedded in STO. Our XAS analysis confirms the metallic nature of the CoPt phase and provides strong evidence for the absence of oxide or compound formation. However, in contrast to other well established growth strategies, such as low energy cluster deposition for example, the present synthesis approach gives rise to a metallic CoPt nanoalloy phase presenting several interesting properties. Its two most striking features are the complete absence of chemical ordering, even after additional annealing steps (note that the temperatures used in the present study generally give rise to pronounced ordering in CoPt nanostructures [27,45,61]) and the large degree of structural disorder, which is linked to strong nanocrystalline texturing. While for low Co concentrations, several different fcc orientations coexist, higher Co concentrations give rise to an additional hcp phase, which is confirmed by magnetometry measurements.

Unfortunately, our growth and annealing temperatures were limited to $T \lesssim 670\,°\text{C}$. In bulk $Co_{50}Pt_{50}$, temperatures up to $\simeq 825\,°\text{C}$ can be used to achieve $L1_0$ ordering. It is therefore conceivable that the system remained stuck in a metastable configuration. However, past work has clearly emphasized the impact of size on the order-disorder phase transition in CoPt nanoalloys. In a seminal study, Alloyeau *et al.* demonstrated a pronounced depression of the order-disorder transition temperature, which, for particles in the size range 2.4–3 nm, was found between $500\,°\text{C}$ and $650\,°\text{C}$ [29]. In the light of these observations, an additional temperature increase would not allow us to achieve further ordering in our nanocomposite system. Thus, in contrast to what has been observed when encapsulating CoPt into amorphous carbon [61], growing nanoalloys using vertical epitaxy might have a strong impact on their structural and thermodynamic properties. To what extent the present results might be generalized to other types of bimetallic ordered phases (CuAu or FePt), when embedded into a single crystal oxide matrix, remains to be fully elucidated.

[1] A. Meldrum, Jr., R. F. Haglund, L. A. Boatner, and C. W. White, Nanocomposite materials formed by ion implantation, Adv. Mater. **13**, 1431 (2001).

[2] M. Gaudry, J. Lermé, E. Cottancin, M. Pellarin, J. L. Vialle, M. Broyer, B. Prével, M. Treilleux, and P. Mélinon, Optical properties of $(Au_xAg_{x-1})_n$ clusters embedded in alumina:

Evolution with size and stoichiometry, Phys. Rev. B **64**, 085407 (2001).

[3] G. Celep, E. Cottancin, J. Lermé, M. Pellarin, L. Arnaud, J. R. Huntzinger, J. L. Vialle, M. Broyer, B. Palpant, O. Boisron, and P. Mélinon, Optical properties of copper clusters embedded in alumina: An experimental and theoretical study of size dependence, Phys. Rev. B **70**, 165409 (2004).

[4] V. Sai K. Chakravadhanula, Y. K. Mishra, V. G. Kotnur, D. K. Avasthi, T. Strunskus, V. Zaporotchenko, D. Fink, L. Kienle, and F. Faupel, Microstructural and plasmonic modifications in Ag-TiO$_2$ and Au-TiO$_2$ nanocomposites through ion beam irradiation, Beilstein J. Nanotechnol. **5**, 1419 (2014).

[5] X. Hu, D. G. Cahill, and R. S. Averback, Burrowing of Pt nanoparticles into SiO$_2$ during ion-beam irradiation, J. Appl. Phys. **92**, 3995 (2002).

[6] A. Klimmer, P. Ziemann, J. Biskupek, U. Kaiser, and M. Flesch, Size-dependent effect of ion bombardment on Au nanoparticles on top of various substrates: Thermodynamically dominated capillary forces versus sputtering, Phys. Rev. B **79**, 155427 (2009).

[7] Udai B. Singh, D. C. Agarwal, S. A. Khan, S. Mohapatra, H. Amekura, D. P. Datta, Ajay Kumar, R. K. Choudhury, T. K. Chan, Thomas Osipowicz, and D. K. Avasthi, Synthesis of embedded Au nanostructures by ion irradiation: Influence of ion induced viscous flow and sputtering, Beilstein J. Nanotechnol. **5**, 105 (2014).

[8] M. Hennes, A. M. Jakob, F. Lehnert, U. Ross, A. Lotnyk, and S. G. Mayr, Nanometer-resolved quantification of mechanical response in nanoparticle-based composites, Nanoscale **8**, 9398 (2016).

[9] M. Mäder, T. Höche, J. W. Gerlach, S. Perlt, J. Dorfmüller, M. Saliba, R. Vogelgesang, K. Kern, and B. Rauschenbach, Plasmonic activity of large-area gold nanodot arrays on arbitrary substrates, Nano Lett. **10**, 47 (2010).

[10] D. J. Sellmyer, M. Zheng, and R. Skomski, Magnetism of Fe, Co and Ni nanowires in self-assembled arrays, J. Phys.: Condens. Matter **13**, R433 (2001).

[11] J. Yao, Z. Liu, Y. Liu, Y. Wang, C. Sun, G. Bartal, A. M. Stacy, and X. Zhang, Optical negative refraction in bulk metamaterials of nanowires, Science **321**, 930 (2008).

[12] M. Hennes, V. Schuler, X. Weng, J. Buchwald, D. Demaille, Y. Zheng, and F. Vidal, Growth of vertically aligned nanowires in metal–oxide nanocomposites: Kinetic monte-carlo modeling versus experiments, Nanoscale **10**, 7666 (2018).

[13] L. Mohaddes-Ardabili, H. Zheng, S. B. Ogale, B. Hannoyer, W. Tian, J. Wang, S. E. Lofland, S. R. Shinde, T. Zhao, Y. Jia, L. Salamanca-Riba, D. G. Schlom, M. Wuttig, and R. Ramesh, Self-assembled single-crystal ferromagnetic iron nanowires formed by decomposition, Nat. Mater. **3**, 533 (2004).

[14] F. Vidal, Y. Zheng, J. Milano, D. Demaille, P. Schio, E. Fonda, and B. Vodungbo, Nanowires formation and the origin of ferromagnetism in a diluted magnetic oxide, Appl. Phys. Lett. **95**, 152510 (2009).

[15] F. Vidal, Y. Zheng, P. Schio, F. J. Bonilla, M. Barturen, J. Milano, D. Demaille, E. Fonda, A. J. A. de Oliveira, and V. H. Etgens, Mechanism of Localization of the Magnetization Reversal in 3 nm Wide Co Nanowires, Phys. Rev. Lett. **109**, 117205 (2012).

[16] P. Schio, F. J. Bonilla, Y. Zheng, D. Demaille, J. Milano, A. J. A. de Oliveira, and F. Vidal, Grain structure and magnetic

relaxation of self-assembled Co nanowires, J. Phys.: Condens. Matter **25**, 056002 (2013).

[17] J. Huang, L. Li, P. Lu, Z. Qi, X. Sun, X. Zhang, and H. Wang, Self-assembled Co-BaZrO$_3$ nanocomposite thin films with ultra-fine vertically aligned Co nanopillars, Nanoscale **9**, 7970 (2017).

[18] V. Schuler, F. J. Bonilla, D. Demaille, A. Coati, A. Vlad, Y. Garreau, M. Sauvage-Simkin, A. Novikova, E. Fonda, S. Hidki, V. Etgens, F. Vidal, and Y. Zheng, Huge metastable axial strain in ultrathin heteroepitaxial vertically aligned nanowires, Nano Res. **8**, 1964 (2015).

[19] Q. Su, W. Zhang, P. Lu, S. Fang, F. Khatkhatay, J. Jian, L. Li, F. Chen, X. Zhang, J. L. MacManus-Driscoll, A. Chen, Q. Jia, and H. Wang, Self-assembled magnetic metallic nanopillars in ceramic matrix with anisotropic magnetic and electrical transport properties, ACS Appl. Mater. Interfaces **8**, 20283 (2016).

[20] X. Weng, M. Hennes, A. Coati, A. Vlad, Y. Garreau, M. Sauvage-Simkin, E. Fonda, G. Patriarche, D. Demaille, F. Vidal, and Y. Zheng, Ultrathin Ni nanowires embedded in SrTiO$_3$: Vertical epitaxy, strain relaxation mechanisms, and solid-state amorphization, Phys. Rev. Materials **2**, 106003 (2018).

[21] L. Li, L. Sun, J. S. Gomez-Diaz, N. L. Hogan, P. Lu, F. Khatkhatay, W. Zhang, J. Jian, J. Huang, Q. Su, M. Fan, C. Jacob, J. Li, X. Zhang, Q. Jia, M. Sheldon, A. Alu, X. Li, and H. Wang, Self-assembled epitaxial Au–oxide vertically aligned nanocomposites for nanoscale metamaterials, Nano Lett. **16**, 3936 (2016).

[22] S. Kawasaki, R. Takahashi, T. Yamamoto, M. Kobayashi, H. Kumigashira, J. Yoshinobu, F. Komori, A. Kudo, and M. Lippmaa, Photoelectrochemical water splitting enhanced by self-assembled metal nanopillars embedded in an oxide semiconductor photoelectrode, Nat. Commun. **7**, 11818 (2016).

[23] M. Lippmaa, S. Kawasaki, R. Takahashi, and T. Yamamoto, Noble metal clustering and nanopillar formation in an oxide matrix, Jpn. J. Appl. Phys. **59**, 010501 (2019).

[24] F. J. Bonilla, A. Novikova, F. Vidal, Y. Zheng, E. Fonda, D. Demaille, V. Schuler, A. Coati, A. Vlad, Y. Garreau, M. S. Simkin, Y. Dumont, S. Hidki, and V. Etgens, Combinatorial growth and anisotropy control of self-assembled epitaxial ultrathin alloy nanowires, ACS Nano **7**, 4022 (2013).

[25] V. Schuler, J. Milano, A. Coati, A. Vlad, M. Sauvage-Simkin, Y. Garreau, D. Demaille, S. Hidki, A. Novikova, E. Fonda, Y. Zheng, and F. Vidal, Growth and magnetic properties of vertically aligned epitaxial CoNi nanowires in (Sr, Ba)TiO$_3$ with diameters in the 1.8-6 nm range, Nanotechnology **27**, 495601 (2016).

[26] P. Andreazza, V. Pierron-Bohnes, F. Tournus, C. Andreazza-Vignolle, and V. Dupuis, Structure and order in cobalt/platinum-type nanoalloys: From thin films to supported clusters, Surf. Sci. Rep. **70**, 188 (2015).

[27] K. Barmak, R. A. Ristau, K. R. Coffey, M. A. Parker, and J. K. Howard, Grain growth and ordering kinetics in CoPt thin films, J. Appl. Phys. **79**, 5330 (1996).

[28] R. A. Ristau, K. Barmak, L. H. Lewis, K. R. Coffey, and J. K. Howard, On the relationship of high coercivity and L1$_0$ ordered phase in CoPt and FePt thin films, J. Appl. Phys. **86**, 4527 (1999).

[29] D. Alloyeau, C. Ricolleau, C. Mottet, T. Oikawa, C. Langlois, Y. Le Bouar, N. Braidy, and A. Loiseau, Size and shape effects on

the order-disorder phase transition in CoPt nanoparticles, Nat. Mater. **8**, 940 (2009).

[30] L. Favre, V. Dupuis, E. Bernstein, P. Mélinon, A. Pérez, S. Stanescu, T. Epicier, J.-P. Simon, D. Babonneau, J.-M. Tonnerre, and J.-L. Hodeau, Structural and magnetic properties of CoPt mixed clusters, Phys. Rev. B **74**, 014439 (2006).

[31] A. Ouerghi, J. Penuelas, C. Andreazza-Vignolle, P. Andreazza, N. Bouet, and H. Estrade-Szwarckopf, Chemical and structural aspects of CoPt silicide nanostructures grown on Si(100), J. Appl. Phys. **100**, 124310 (2006).

[32] R. K. Rakshit, S. K. Bose, R. Sharma, and R. C. Budhani, Giant coercivity nanodots and fractals in CoPt films grown on (001) $SrTiO_3$ using pulsed laser deposition, Appl. Phys. Lett. **89**, 202511 (2006).

[33] D. Suzuki, M. Ohtake, F. Kirino, and M. Futamoto, Preparation of CoPt-alloy thin films with perpendicular magnetic anisotropy on MgO(111), $SrTiO_3$(111), and Al_2O_3(0001) single-crystal substrates, IEEE Trans. Magn. **48**, 3195 (2012).

[34] A. Itabashi, M. Ohtake, S. Ouchi, F. Kirino, and M. Futamoto, Structure characterization of FePd, FePt, and CoPt alloy thin films epitaxially grown on $SrTiO_3$(001) single-crystal substrates, J. Magn. Soc. Jpn. **37**, 202 (2013).

[35] J. Buchwald and M. Hennes, Adsorption and diffusion of Au, Pt, and Co adatoms on $SrTiO_3$(001) surfaces: A density functional theory study, Surf. Sci. **701**, 121683 (2020).

[36] S. Plimpton, Fast parallel algorithms for short-range molecular dynamics, J. Comput. Phys. **117**, 1 (1995).

[37] B.-J. Lee and M. I. Baskes, Second nearest-neighbor modified embedded-atom-method potential, Phys. Rev. B **62**, 8564 (2000).

[38] J.-S. Kim, D. Seol, J. Ji, H.-S. Jang, Y. Kim, and B.-J. Lee, Second nearest-neighbor modified embedded-atom method interatomic potentials for the Pt-M (M= Al, Co, Cu, Mo, Ni, Ti, V) binary systems, Calphad **59**, 131 (2017).

[39] W. Shinoda, M. Shiga, and M. Mikami, Rapid estimation of elastic constants by molecular dynamics simulation under constant stress, Phys. Rev. B **69**, 134103 (2004).

[40] M. E. Tuckerman, J. Alejandre, R. López-Rendón, A. L. Jochim, and G. J. Martyna, A Liouville-operator derived measure-preserving integrator for molecular dynamics simulations in the isothermal-isobaric ensemble, J. Phys. A: Math. Gen. **39**, 5629 (2006).

[41] E. K. Hlil, R. Baudoing-Savois, B. Moraweck, and A. J. Renouprez, X-ray absorption edges in platinum-based alloys. 2. influence of ordering and of the nature of the second metal, J. Phys. Chem. **100**, 3102 (1996).

[42] Y. S. Lee, J. Y. Rhee, C. N. Whang, and Y. P. Lee, Electronic structure of Co-Pt alloys: X-ray spectroscopy and density-functional calculations, Phys. Rev. B **68**, 235111 (2003).

[43] M. Kuhn, T. K. Sham, J. M. Chen, and K. H. Tan, Electronic structure of Cu_3Au from the Cu viewpoint, Solid State Commun. **75**, 861 (1990).

[44] B. Moraweck, A. J. Renouprez, E. K. Hlil, and R. Baudoing-Savois, Alloying effects on x-ray absorption edges in nickel-platinum single crystals, J. Phys. Chem. **97**, 4288 (1993).

[45] N. Blanc, L. E. Díaz-Sánchez, A. Y. Ramos, F. Tournus, H. C. N. Tolentino, M. De Santis, O. Proux, A. Tamion, J. Tuaillon-Combes, L. Bardotti, O. Boisron, G. M. Pastor, and V. Dupuis, Element-specific quantitative determination of the local atomic order in CoPt alloy nanoparticles: Experiment and theory, Phys. Rev. B **87**, 155412 (2013).

[46] M. Brown, R. E. Peierls, and E. A. Stern, White lines in x-ray absorption, Phys. Rev. B **15**, 738 (1977).

[47] N. M. Souza-Neto, A. Y. Ramos, H. C. N. Tolentino, and Y. Joly, Depth dependent local structures in CoPt thin films, J. Phys.: Conf. Ser. **190**, 012112 (2009).

[48] G. Bunker, *Introduction to XAFS* (Cambridge University Press, Cambridge, 2010).

[49] B. Ravel and M. Newville, ATHENA, ARTEMIS, HEPHAESTUS: Data analysis for x-ray absorption spectroscopy using IFEFFIT, J. Synchrotron Radiat. **12**, 537 (2005).

[50] R. Giulian, L. L. Araujo, P. Kluth, D. J. Sprouster, C. S. Schnohr, G. J. Foran, and M. C. Ridgway, Temperature-dependent EXAFS analysis of embedded Pt nanocrystals, J. Phys.: Condens. Matter **21**, 155302 (2009).

[51] David J. Sprouster and Mark C. Ridgway, Ion beam formation and modification of cobalt nanoparticles, Appl. Sci. **2**, 396 (2012).

[52] D. J. Sprouster, R. Giulian, L. L. Araujo, P. Kluth, B. Johannessen, N. Kirby, K. Nordlund, and M. C. Ridgway, Ion-irradiation-induced amorphization of cobalt nanoparticles, Phys. Rev. B **81**, 155414 (2010).

[53] H. Magnan, D. Chandesris, G. Rossi, G. Jezequel, K. Hricovini, and J. Lecante, Determination of the local order in amorphous cobalt films, Phys. Rev. B **40**, 9989 (1989).

[54] G. Apai, J. F. Hamilton, J. Stohr, and A. Thompson, Extended x-ray—Absorption Fine Structure of Small Cu And Ni Clusters: Binding-Energy and Bond-Length Changes with Cluster Size, Phys. Rev. Lett. **43**, 165 (1979).

[55] G. Radtke, M. Hennes, M. Bugnet, Q. M. Ramasse, X. Weng, D. Demaille, B. Gobaut, P. Ohresser, E. Otero, F. Choueikani, A. Juhin, P. Sainctavit, Y. Zheng, and F. Vidal, Atomic-scale study of metal–oxide interfaces and magnetoelastic coupling in self-assembled epitaxial vertically aligned magnetic nanocomposites, Adv. Mater. Interfaces **6**, 1900549 (2019).

[56] M. Hennes, X. Weng, E. Fonda, B. Gallas, G. Patriarche, D. Demaille, Y. Zheng, and F. Vidal, Phase separation and surface segregation in Co−Au−SrTiO_3 thin films: Self-assembly of bilayered epitaxial nanocolumnar composites, Phys. Rev. Materials **3**, 035002 (2019).

[57] S. S. A. Razee, J. B. Staunton, and F. J. Pinski, First-principles theory of magnetocrystalline anisotropy of disordered alloys: Application to cobalt platinum, Phys. Rev. B **56**, 8082 (1997).

[58] F. Ono, Magnetic field dependence of the magnetocrystalline anisotropy energy in hcp Co, J. Phys. Soc. Jpn. **50**, 2564 (1981).

[59] F. Bolzoni, F. Leccabue, R. Panizzieri, and L. Pareti, Magnetocrystalline anisotropy and phase transformation in Co–Pt alloy, IEEE Trans. Magn. **20**, 1625 (1984).

[60] R. C. O'Handley, *Modern Magnetic Materials* (Wiley, New York, 2000).

[61] F. Tournus, A. Tamion, N. Blanc, A. Hannour, L. Bardotti, B. Prével, P. Ohresser, E. Bonet, T. Epicier, and V. Dupuis, Evidence of $L1_0$ chemical order in CoPt nanoclusters: Direct observation and magnetic signature, Phys. Rev. B **77**, 144411 (2008).